PAPER

Check for updates

Corrosion resistance of Ni–P/SiC and Ni–P composite coatings prepared by magnetic field-enhanced jet electrodeposition

Xiuqing Fu, [ID] *[ab] Feixiang Wang,[a] Xinxin Chen,[a] Jinran Lin[a] and Hongbing Cao[a]

To extend the working life of 45# steel, Ni–P and Ni–P/SiC composite coatings were prepared on its surface by magnetic field-enhanced jet electrodeposition. This study investigated the effect of magnetic field on the corrosion resistance of Ni–P and Ni–P/SiC composite coatings prepared by conventional jet electrodeposition. The surface and cross-sectional morphologies, microstructure, and composition of the composite coatings were determined by scanning electron microscopy (SEM), energy dispersive spectrometry (EDS), and X-ray diffraction (XRD), respectively. The corrosion resistance was studied using a LEXT4100 laser confocal microscope. The introduction of a stable magnetic field was found to improve the surface morphology of the coatings, increase the growth rate, and reduce the agglomeration of nano-SiC (3 g L^{-1}, 40 nm) particles, thus significantly improving the corrosion resistance of the coatings. The corrosion potential of the Ni–P coating increased from -0.78 V (0 T) to -0.46 V (0.5 T), and the corrosion current density decreased from 9.56×10^{-6} A dm^{-2} (0 T) to 4.31×10^{-6} A dm^{-2} (0.5 T). The corrosion potential of the Ni–P/SiC coating increased from -0.59 V (0 T) to -0.28 V (0.5 T), and the corrosion current density decreased from 6.01×10^{-6} A dm^{-2} (0 T) to 2.90×10^{-6} A dm^{-2} (0.5 T).

1. Introduction

45# steel, which is widely used in machinery, has a high hardness and resistance to deformation.[1–3] However, it is prone to corrosion under the influence of the external environment, which decreases the actual working life and application.[4,5] Applying a protective coating on steel substrates is an important measure to prevent steel corrosion, and nickel-base alloy coatings are the most widely studied and applied chemical coatings.[6–8] Latest research has shown that conventional nickel-base coatings do not meet the requirements of the industry. Currently, many scholars are focusing on methods to improve the properties of conventional nickel-base alloy coatings.

In recent years, studies have shown that the co-deposition of insoluble second-phase particles into a coating can improve its performance.[9–12] For example, nano-SiC particles, which have a high oxidation resistance and stability,[13–15] have been used to prepare Ni–SiC composite coatings by co-deposition with Ni ions in the plating solution.[16,17] However, nano-SiC particles easily agglomerate and affect the coating performance.[18–20] Currently, research on the agglomeration of nano-SiC particles is mainly conducted in terms of the bath parameters,[21] current

magnitude,[22,23] and stirring mode, with techniques such as rotating composite electrodeposition and magnetic composite electrodeposition.[17,24,25] The jet electrodeposition technology is a new and improved version of the conventional electrodeposition method. Compared with the conventional method, jet electrodeposition has advantages of selectivity and fast deposition. The surface of an alloy coating produced by jet electrodeposition is more uniform and has a better performance.[26,27] However, the coatings prepared by jet electrodeposition often contain defects, such as pits, bulges, and unevenness, which affect their corrosion resistance. With developments in the field of magnetoelectrochemistry, many scholars have studied the application of a magnetic field during the electrodeposition process. They found that the coating properties can be significantly improved under the action of a magnetic field. To improve the corrosion resistance of coatings, an experiment on jet electrodeposition enhanced by the application of a magnetic field was conducted by introducing a magnetic field platform.

In this study, Ni–P (no magnetic field; parallel magnetic field: 0.5 T) and Ni–P/SiC coatings (no magnetic field; parallel magnetic field: 0.5 T) were prepared. The microscopic appearance and element contents of the coatings were analyzed by scanning electron microscopy (SEM) and energy dispersive spectrometry (EDS) to explore their influence on the corrosion resistance of the coatings. The corrosion resistances of Ni–P and Ni–P/SiC coatings were determined by conducting an electrochemical test.

[a]College of Engineering, Nanjing Agricultural University, Nanjing 210031, P. R. China. E-mail: fuxiuqing@njau.edu.cn; Tel: +86-1391-387-8179

[b]Key Laboratory of Intelligence Agricultural Equipment of Jiangsu Province, Nanjing 210031, P. R. China

2. Experiment

2.1 Experimental device

Fig. 1a shows a schematic of the jet electrodeposition system. As shown, a nickel rod is connected to the positive electrode of the power supply and mounted onto the nozzle of the machine tool spindle. The workpiece is connected to the negative electrode of the power supply and installed on the workpiece installation platform below the nozzle. After the power is switched on, the nozzle reciprocates during the working process. The anode nickel rod, plating solution, and cathode workpiece form a closed loop to realize ion deposition. The magnetic platform is made of NdFeB and installed on the workpiece installation platform, providing a stable and constant magnetic field horizontal to the direction of the electric field during the jet electrodeposition process.

2.2 Experimental content and parameters

The base material was a 45# steel workpiece (25 mm × 10 mm × 8 mm), sanded with 320#, 800#, and 2000# sandpapers until a reflective surface appeared ($R_a \leq 0.1$). The workpiece was placed in anhydrous ethanol for ultrasonic cleaning. Based on a previous experiment,[28,29] the following values of the operating parameters were selected for preparing the Ni–P and Ni–P/SiC coatings by jet electrodeposition: a processing current density of 24 A dm^{-2}, a bath temperature of 60 °C, a processing time of 25 min, and a bath flow rate of 4.5 m s^{-1}. Table 1 lists the composition and content of the plating solution. The magnetic platform provided a stable magnetic field with a magnetic flux density of 0.5 T. Before jet electrodeposition, the workpiece was pretreated as follows: electric deoiling → weak activation → strong activation. The nano-SiC particles used in the experiment were purchased from Shanghai Yaotian New Material Technology Co., Ltd. The purity was 99.9%, and the size of the nanoparticles was 40 nm. To evenly distribute the nano-SiC particles in the plating solution, the plating solution was magnetically stirred (for 5 h at a rotor speed of 400 rpm and a stirring temperature of 25 °C) to keep the particles suspended and to prevent them from settling or floating.[30,31]

Fig. 1 Ni–P and Ni–P/SiC composite coating preparation: (a) schematic of conventional jet electrodeposition, (b) actual image of the apparatus, and (c) schematic of parallel magnetic field-enhanced jet electrodeposition system.

Table 1 Plating solution composition

Chemical reagent	Content (g L^{-1})
NiSO$_4\cdot$6H$_2$O	200
NiCl$_2\cdot$6H$_2$O	30
H$_3$PO$_3$	20
H$_3$BO$_3$	30
C$_6$H$_8$O$_7$	60
CH$_4$N$_2$S	0.01
C$_{12}$H$_{25}$SO$_4$Na	0.08
SiC (40 nm)	3

2.3 Test instrument

A Quanta FEG250 scanning electron microscope (FEI instruments, Oregon, USA) was used to observe the surface and cross-sectional morphologies of the coatings. The accelerating voltage and scanning rate were 15 kV and 30 μs, respectively. The XFlash 5030 EDS energy spectrum analyzer (Berlin Bruker AXS, Germany) was used to measure the elements and their contents in the coatings, at an accelerating voltage of 16 kV and a scanning area of 1 mm^2. The PANalytical X′Pert X-ray diffractometer was used to analyze the phase structure composition of the coatings. The working voltage was 40 kV, the scanning rate was 5° min^{-1}, and the scanning range was 10°–100°. The electrochemical workstation CS350 (Wuhan Corrtest Instrument Co., Ltd.) was used to test the corrosion resistance of the workpiece. In the experiment, the electrochemical workstation comprised three electrodes: a workpiece electrode, platinum (Pt) electrode, and saturated calomel electrode (SCE). In the detection process, the workpiece surface was insulated, and epoxide resin was used to wrap its surface, while exposing an area of 1 cm^2 of the composite coating to be measured. The workpiece was soaked in a 3.5 wt% NaCl solution for 30 min, following which the open-circuit potentials of all the samples entered the stable state. The polarization curves of the coatings were then obtained using the dynamic potential scanning method at a scanning rate of 1 mV s^{-1}. Subsequently, the self-corrosion potential and self-corrosion current parameters of the corrosion resistance were determined using the epitaxial method. Electrochemical impedance spectroscopy (EIS) in the alternating current mode was applied to measure the impedance spectrum of the coating immersed in the corrosive medium at the open circuit potential. The test frequency range was 10^{-2} to 10^{-5} Hz, swept from high to low. The ZSimpWin software was used for the fitting analysis of the obtained impedance spectrum.

3. Results and discussion

3.1 Surface morphologies

Fig. 2 shows the surface morphologies of the Ni–P and Ni–P/SiC composite coatings. As shown, Ni and P deposit and form a solid solution induced by the catalytic activator on the cathode surface. Their growth follows the 2D crystal core growth model. As the deposition proceeds, the coating surface exhibits
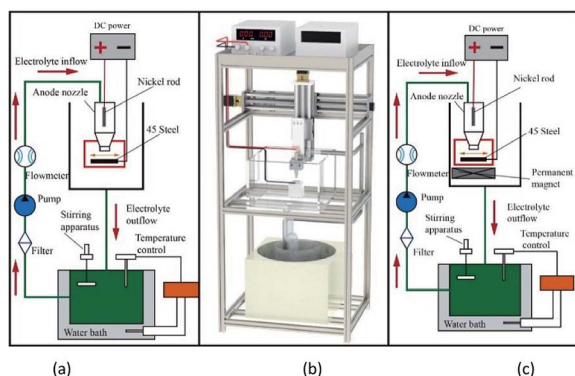
a typical cellular structure.[32] Fig. 2a shows the surface morphology of the Ni–P composite coating (0 T), where the cellular structure on the coating surface is relatively evident. The surface roughness of the coating is poor, and there are evident pits, projections, holes, and cracks. This is mainly because, in the process of jet electrodeposition, the bubbles produced by the hydrogen evolution reaction on the cathode surface adhere to the cathode surface.[33] The crystal cells in the composite coating grow rapidly, so a lot of hydrogen is trapped in the composite coating, and pits and holes are easily formed on the surface. Moreover, in the deposition process, because the cathode surface is not ideally flat, the local uneven deposition will cause protrusions. Compared with the smoother parts, the curvature at the front end of the protrusion is larger, and the charge density is higher.[34] The intensity of the electric field near the protrusions is higher than that in the other regions, thus producing a tip effect. The uneven deposition at this point is also amplified by the tip effect, resulting in bulges and cracks, as shown in the figure. Fig. 2b shows the surface morphology of the Ni–P composite coating (0.5 T). The surface morphology in this case is improved, and the cellular structure boundary is fuzzy. Compared with the surface morphology of the Ni–P composite coating (0 T), the cellular structure is flattened, the flatness of the coating is improved, and the surface quality is better.

Fig. 2c shows the surface morphology of the Ni–P/SiC composite coating (0 T). The boundary between the cellular structures can still be clearly observed on the coating surface. Although pits, bumps, holes, and other defects remain on the surface, the coating quality is improved compared with the Ni–P (0 T) composite coating (0 T). Moreover, there are some agglomerated nano-SiC particles on the coating surface. It is concluded that the addition of nano-SiC particles increased the nucleation sites of nickel phosphorus per unit area, improved the nucleation rate of the coating, and thus refined the grains.[35] A flat and compact surface morphology can help reduce the porosity and improve the corrosion resistance of coatings. However, the agglomeration of nano-SiC particles in the electroplating solution was evident. With the co-deposition, the agglomerated nano-SiC particles were scattered on the surface of the Ni–P/SiC composite coating (0 T) with poor binding and were not well embedded in the composite coating. The agglomerated particles easily fell off and formed pits after being corroded, leaving the coating unprotected.[36] Fig. 2d shows the surface morphology of the Ni–P/SiC composite coating (0.5 T). After the addition of the magnetic field, the Ni–P/SiC composite coating (0.5 T) exhibits a compact surface structure, a compact cellular structure, and a fuzzy boundary. No evident defects can be found on the coating surface. It is concluded that the cathode surface was not completely flat and that protrusions would have formed during the deposition. The current will deviate on the surface of the protrusions, causing it to produce a component parallel to the magnetic field and a component perpendicular to it. In this case, eddy currents are generated at the front of the protrusions. With the increase in the magnetic flux density, the eddy current intensity will be further enhanced.[37,38] Moreover, as the cathode material is a soft
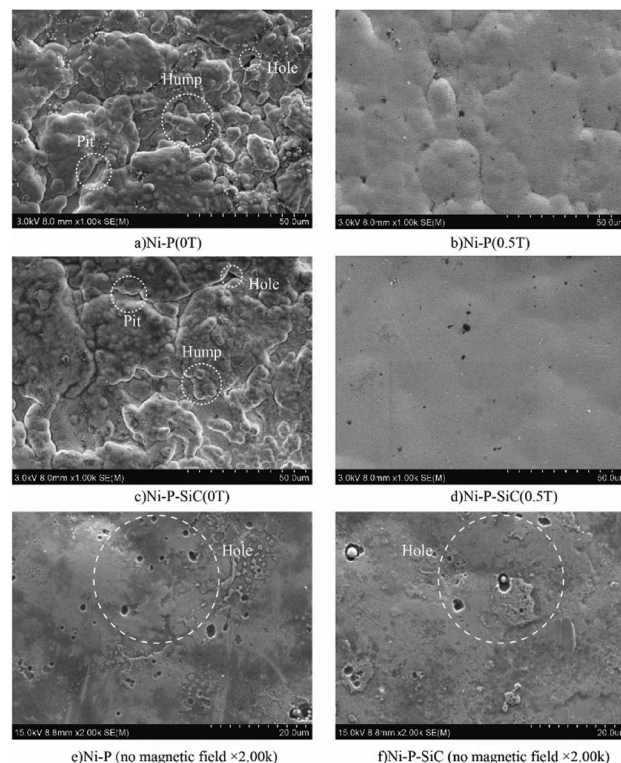

Fig. 2 Surface micromorphologies of Ni–P and Ni–P/SiC composite coatings: (a) Ni–P (0 T), (b) Ni–P (0.5 T), (c) Ni–P/SiC (0 T), (d) Ni–P/SiC (0.5 T), (e) Ni–P (no magnetic field × 2.00 K) and (f) Ni–P/SiC (no magnetic field × 2.00 K).

magnetic material, a higher gradient magnetic field will be generated at the front end of the protrusions, thereby further enhancing the magnetohydrodynamics (MHD) effect. Under the combined action of the gradient magnetic field force and MHD effect, a scour effect is produced, which hinders the growth of the "needle-like" protrusions and makes the protrusion front
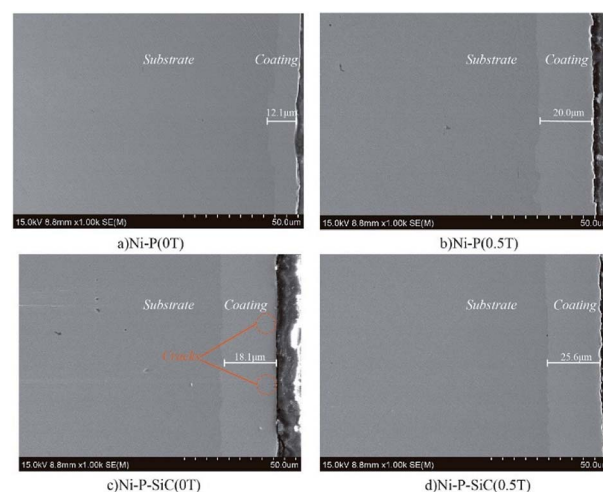

Fig. 3 Cross-sectional morphologies of the Ni–P and Ni–P/Sic composite coatings: (a) Ni–P (0 T), (b) Ni–P (0.5 T), (c) Ni–P/SiC (0 T), and (d) Ni–P/SiC (0.5 T).

Table 2 Coating thickness and growth rate

Type of coating	Coating thickness (μm)	Growth rate of coating (μm min^{-1})
Ni–P (0 T)	12.1	0.484
Ni–P (0.5 T)	20.0	0.800
Ni–P/SiC (0 T)	18.1	0.724
Ni–P/SiC (0.5 T)	25.6	1.024

flat.[39] In the middle of the vortex, the flow rate is relatively low. Therefore, the nano-SiC particles are more concentrated at the middle of the protrusions. The coating can wrap the nano-particles well and make each cellular structure more uniform. Fig. 2e and f show the magnified views of the cellular structure boundaries of the Ni–P and Ni–P/SiC composite coatings, respectively. As shown, there are some micro-holes on the coating surface, mainly due to the bubbles generated by the hydrogen evolution reaction on the electrode surface during the electrodeposition process, which are adsorbed onto the cathode surface and remain therein before floating upward. With the addition of the parallel magnetic field, the precipitated H$_2$ molecules are also affected by the magnetic field disturbance. The H$_2$ molecules quickly fall off from the surface to be processed. Thus, the quality of the composite coating is improved.

3.2 Cross-sectional morphologies

The section morphology and section thickness of the Ni–P and Ni–P/SiC composite coatings were observed and measured by FEI-SEM. Fig. 3 shows the observation and measurement results. To explore the effect of magnetic field on the growth rate of the coatings, the following formula was used to calculate the growth rate. Table 2 lists the calculation results.

$$V_g = \frac{H_g}{t} \tag{1}$$

where V_g is the growth rate (μm min^{-1}); H_g is the growth thickness of the composite coating (μm); t is the preparation time (min).

Fig. 3a shows the cross-sectional morphology of the Ni–P coating (0 T). There are no evident defects in the composite coating. The thickness of the composite coating is 12.1 μm, and the growth rate is 0.484 μm min^{-1}. Fig. 3b shows the cross-sectional morphology of the Ni–P coating (0.5 T). The coating section is relatively dense, the coating thickness is 20.0 μm, and the growth rate is 0.800 μm min^{-1}. Compared with the Ni–P coating (0 T), the coating thickness and growth rate increased by 65.2%. This is because the Ni and P ions in the bath were affected by the Lorentz force during the deposition under the assistance of the magnetic field. More Ni and P ions were captured on the workpiece surface, which improved the deposition efficiency of the coating.[40]

Fig. 3c shows the cross-sectional morphology of the Ni–P/SiC coating (0 T). There are some cracks in the coating section. This is because nano-SiC particles when few in number do not disperse well in the coating, resulting in a high concentration of local nano-SiC particles and uneven distribution of the internal
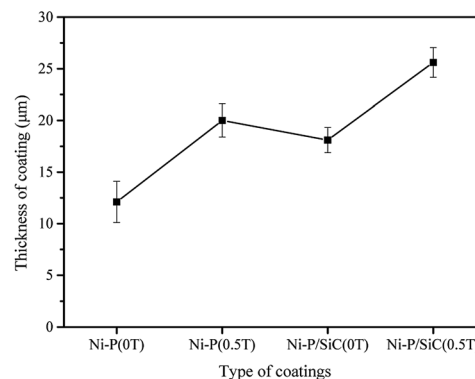

Fig. 4 Thickness of Ni–P and Ni–P/SiC composite coatings.

stress during the growth. The regions with a higher particle concentration grow faster and produce a higher internal stress, thus producing cracks and other defects.[18] In this case, the coating thickness is 18.1 μm, and the growth rate is 0.724 μm min^{-1}. Fig. 3d shows the cross-sectional morphology of the Ni–P/SiC coating (0.5 T). As shown, the coating is dense, and there are no cracks or other defects due to the local uneven distribution of the nano-SiC particles and internal stress concentration. According to Guglielmi's adsorption theory, nanoparticles in a bath are coated with ions. After reaching the cathode surface, they are first loosely absorbed (weakly absorbed) onto the cathode surface, which is a physical adsorption and a reversible process. Second, as the deposition progresses, a part of the ions weakly adsorbed on the particles are reduced, and a strong adsorption (strong adsorption stage) occurs between the particles and the cathode. This process is irreversible, and the particles gradually enter the cathode surface and are then buried by the deposited metal.[41]

In this study, the addition of the magnetic field effectively improved the dispersion degree of the nano-SiC particles in the plating solution. Thus, more nano-SiC particles entered the strong adsorption stage and were uniformly distributed in the coating. As nucleation centers, the nanoparticles provided several nucleation growth points *via* the composite synergy effect, which increased the nucleation rate of the composite coating and promoted the formation of new grains while
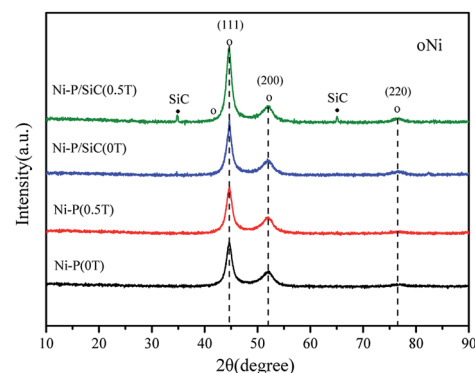

Fig. 5 XRD patterns of the Ni–P and Ni–P/SiC composite coatings.

Table 3 Element content and grain size of the coatings

Type of coating	P content (at%)	Si content (at%)	Grain size (nm)	Crystallinity (%)
Ni–P (0 T)	4.3	—	6.9	69.65
Ni–P (0.5 T)	6.5	—	5.9	77.21
Ni–P/SiC (0 T)	4.6	1.4	6.1	79.64
Ni–P/SiC (0.5 T)	7.0	6.0	4.8	77.78

inhibiting the growth of the formed grains. Thus, the coating was more compact. As shown in Fig. 4, the coating thickness reached 25.6 μm, and the growth rate was 1.024 μm min⁻¹, which is 41.4% higher than that of the coating prepared by jet electrodeposition.

3.3 Coating structure and composition

Fig. 5 shows the XRD patterns of the Ni–P and Ni–P/SiC composite coatings, including a comparison with the standard PDF card. As shown, the Ni–P composite coating exhibits broad diffusion peaks around $2\theta = 45°$, $52°$, and $77°$, which are (111), (200), and (220) characteristic XRD peaks, respectively. The three main peaks are sharp at the top and wide at the bottom, indicating that the composite coating is composed of a mixture of crystalline and amorphous phases, all of which are face-centered cubic structures. Table 3 presents the grain size of the Ni (111) crystal plane, calculated using the Scherrer formula.[42] The grain size of the Ni (111) crystal plane in the Ni–P (0 T) composite coating is 7.2 nm. After the addition of the magnetic field, the micro-MHD effect on the cathode surface accelerates the transfer of the charged ions and thus increases the nucleation efficiency. The surface grains on the cathode are refined with the increase in the nucleation rate. Therefore, the grain size of the Ni (111) crystal plane in the Ni–P (0.5 T) composite coating is reduced to 5.8 nm. The XRD pattern of the Ni–P/SiC (0 T) composite coating shows no characteristic peak of SiC, and the grain size of the Ni (111) crystal plane in the Ni–P/SiC (0 T) composite coating is 6.1 nm. With the addition of the magnetic field, the Ni–P/SiC (0.5 T) composite coating begins to show a sharp SiC crystal peak in the XRD pattern. However, the characteristic peaks of Ni and P (XRD) do not change significantly. This is because the nano-SiC particles were mechanically embedded in the coating. Moreover, it can be proven that the coating exhibits an amorphous structure. As the content of nano-SiC particles increases, the nucleation rate of the coating increases, and the grains are further refined. At this point, the grain size of the Ni (111) element in the coating reaches the minimum value of 4.8 nm, and the effect of grain refinement is most evident. The Jade 6 software was used to analyze and calculate the grain size and crystallinity. The ratio of the area of all the crystal peaks to the total area of all the diffraction peaks represents the crystallinity. The calculation formula is as follows:

$$\text{Crystallinity}(\%) = \frac{S_{\text{crystal peak}}}{S_{\text{total peak}}} \times 100\% \qquad (2)$$
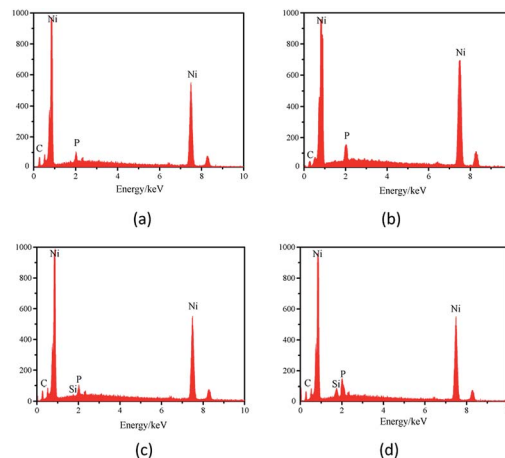

Fig. 6 Line scan measurement results of the Ni–P and Ni–P/SiC coatings: (a) Ni–P (0 T), (b) Ni–P (0.5 T), (c) Ni–P/SiC (0 T), and (d) Ni–P/SiC (0.5 T).

Fig. 6 shows the EDS spectra of the Ni–P and Ni–P/SiC composite coatings, where Ni and P elements can be detected. With the addition of the nano-SiC particles, tiny Si peaks appear in the energy spectra of the coating surface. This indicates a successful preparation of the Ni–P and Ni–P/SiC coatings.

Table 3 lists the P fraction of the Ni–P coating. The P fraction of the coating prepared by conventional jet electrodeposition is 4.30 at%. With the addition of the magnetic field, the P fraction of the coating is increased to 6.45 at%. Fig. 7 shows the SEM surface scanning results of the Ni–P coating (the scanning element is P). As shown, the distribution of the P elements in the Ni–P (0 T) coating is uneven, as indicated by the blank area (area A). The P element content in the Ni–P (0.5 T) coating is increased and is uniformly distributed in the coating. This is
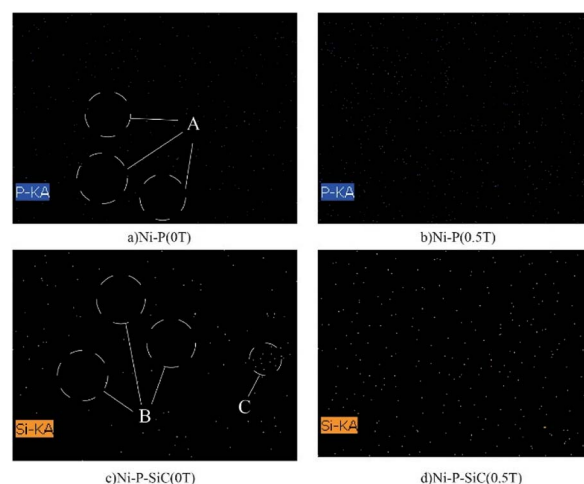

Fig. 7 Surface scanning measurement results of the Ni–P and Ni–P/SiC coatings (A: blank area of P element; B: blank area of Si element; C: concentrated area of Si element): (a) distribution map of P element: Ni–P (0 T) coating, (b) distribution map of P element: Ni–P (0.5 T), (c) distribution map of Si element: Ni–P/SiC (0 T), and (d) distribution map of Si element: Ni–P/SiC (0.5 T).

because the charged ions on the cathode surface changed the flow mass transfer on the substrate surface under the action of the Lorentz force and electric field force; thus, the charged ions fully diffused on the coating surface. Table 3 lists the Si element scores of the Ni–P/SiC coatings. The element composition of the coating shows that the Si element fraction is only related to the nano-SiC particle content. Therefore, the Si element fraction can be considered the nano-SiC particle content in the coating. The Si element fraction of the Ni–P/SiC coating prepared by conventional jet electrodeposition is 1.4 at%. With the addition of the magnetic field, this value is increased to 6.0 at%. Fig. 7 shows the SEM surface scanning results of the Ni–P/SiC composite coating (the scanning element is Si). The Si element content in the Ni–P/SiC (0 T) coating is low, the distribution is uneven, and there are blank areas and Si element gathering areas (areas B and C). After the addition of the magnetic field, the nano-SiC particle content in the Ni–P/SiC (0.5 T) composite coating is increased significantly while maintaining a uniform distribution. This is because the cathode surface produces a micro-MHD effect during the deposition process, which disturbs the machining area. This effectively reduces the polymerization tendency of the nano-SiC particles and makes more nano-SiC particles to wrap around the coating. Moreover, the nano-SiC particles were coated with the ions in the bath. The effect of the Lorentz force changed their trajectory.[43] The distribution uniformity of the nanoparticles in the coating was improved owing to the spiral diffusion around the sediment. Therefore, the addition of the magnetic field had a positive effect on the deposition of the ions and nanoparticles.

3.4 Corrosion resistance

To study the corrosion resistance of the Ni–P and Ni–P/SiC composite coatings, the samples were immersed in a neutral 3.5 wt% NaCl aqueous solution (the exposed area of the sample was 1 cm^2). The dynamic potential polarization (Tafel) and EIS curves were measured. Fig. 8 shows the polarization curves. The Tafel extrapolation method of the polarization curve was used to fit and calculate the self-etching potential (E_{corr}) and self-etching current density (I_{corr}) of each electrochemical parameter, as listed in Table 4. The results show that the Ni–P and Ni–

Table 4 Electrochemical and impedance data of the coatings

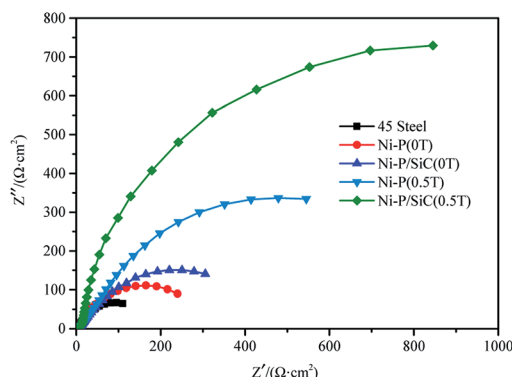| Sample	E_{corr} (V)	i_{corr} (A cm^2)	Corrosion inhibition efficiency (η%)
45# steel	−0.91	2.15×10^{-5}	
Ni–P (0 T)	−0.78	9.56×10^{-6}	57.2
Ni–P (0.5 T)	−0.46	4.31×10^{-6}	68.5
Ni–P/SiC (0 T)	−0.59	6.01×10^{-6}	76.9
Ni–P/SiC (0.5 T)	−0.28	2.90×10^{-6}	87.5

Fig. 9 Nyquist plots of the Ni–P and Ni–P/SiC composite coating.

P/SiC coatings can protect the exposed substrate to some extent, and under the same preparation process, the Ni–P/SiC coatings have a better corrosion resistance. When the magnetic field was added during the coating preparation, the corrosion potential of the coating samples shifted positively, the corrosion current density was reduced, and the corrosion resistance of the coating was improved. Among the prepared coatings, the Ni–P/SiC (0.5 T) coating exhibited the best corrosion resistance, the corrosion voltage (E_{corr}) was −0.226 V, and the corrosion current (I_{corr}) was 2.92×10^{-6} A cm^{-2}. Evidently, the addition of the magnetic field improved the corrosion resistance of the composite coating.

To further study the corrosion resistance of the Ni–P and Ni–P/SiC composite coatings, the EIS method was used to measure the corrosion behavior of each sample in a 3.5 wt% NaCl solution. Nyquist plots were plotted by measuring the impedance spectra of the samples, as shown in Fig. 9. The Ni–P/SiC coating exhibited a better corrosion resistance under the same preparation process. During the preparation of the Ni–P coating, the capacitance impedance arc radius of the composite coating increased significantly. After the addition of the magnetic field in the preparation of the Ni–P/SiC composite coating, the capacitance impedance arc radius of the composite coating increased. Among the prepared coatings, the capacitance impedance arc radius of the Ni–P/SiC (0.5 T) coating was the highest. As a characterization of the electrochemical corrosion behavior of the coating, the higher the capacitance impedance arc radius, the stronger the corrosion resistance of the coating.[44] The corresponding EIS equivalent circuit diagram model was proposed to obtain the sample corrosivity for a quantitative analysis, as shown in Fig. 10, where R_1 is the equivalent
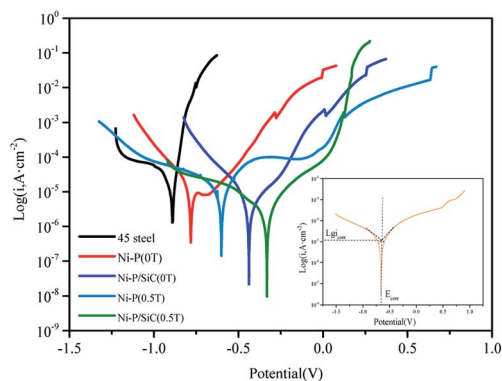

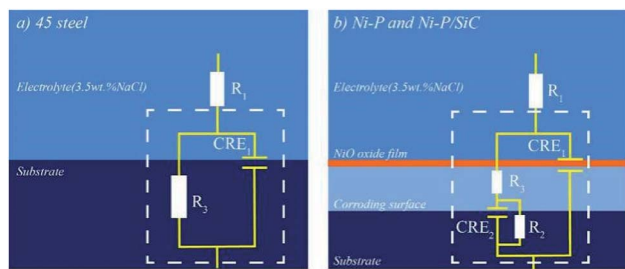**Fig. 8** Potentiodynamic polarization curves of the Ni–P and Ni–P/SiC composite coatings.

Fig. 10 Equivalent circuit diagram model for Ni–P and Ni–P/SiC composite coatings.

Fig. 11 SEM images of the surface micromorphologies of the Ni–P and Ni–P/SiC composite coatings after corrosion test: (a) 45# steel, (b) Ni–P (0 T), (c) Ni–P (0.5 T), (d) Ni–P/SiC (0 T), and (e) Ni–P/SiC (0.5 T).

electrolyte resistance of the NaCl solution, R_2 is the equivalent transfer resistance, and R_3 is the equivalent resistance of the composite coating. A constant phase element (CPE) was used to replace the capacitor in the equivalent circuit to fit the impedance characteristics of the double layer more accurately. CPE_1 corresponds to the film capacitance in the high-frequency region, whereas CPE_2 corresponds to the double-layer capacitance in the low-frequency region. The model contains two time constants: one is the time constant in the high-frequency range composed of CPE_1 and R_3 to characterize the intrinsic properties of the coating, and the other is the time constant in the low-frequency range composed of CPE_2 and charge transfer resistor R_2 and controlled by the charge transfer characterization process. The results were fitted using the ZSimpWin software, as listed in Table 5. The EIS diagram and equivalent circuit were used to fit the equivalent resistance values, and the results show that the Ni–P and Ni–P/SiC coatings could significantly improve the corrosion resistance of the 45# steel. The equivalent resistance value of the Ni–P/SiC composite coating was higher than that of the Ni–P coating under the same process, and the introduction of the magnetic field helped improve the impedance value. The equivalent resistance value of the Ni–P coating improved from 254.70 (0 T) to 632.87 (0.5 T) Ω, and that of the Ni–P/SiC coating improved from 327.02 (0 T) to 1385.89 (0.5 T) Ω.

The morphologies of the Ni–P and Ni–P/SiC composite coatings after corrosion were observed by FEI-SEM. Fig. 11b shows the morphology of the Ni–P (0 T) coating after corrosion. Compared with the morphology of the 45# steel after corrosion (Fig. 11a), the Ni–P coating played a protective role; however, the coating exhibited several cracks and corrosion products on its surface. This is because when an Ni–P composite coating is in contact with air or a corrosive solution, the coating surface is passivated, forming a uniform and dense passivation film. This
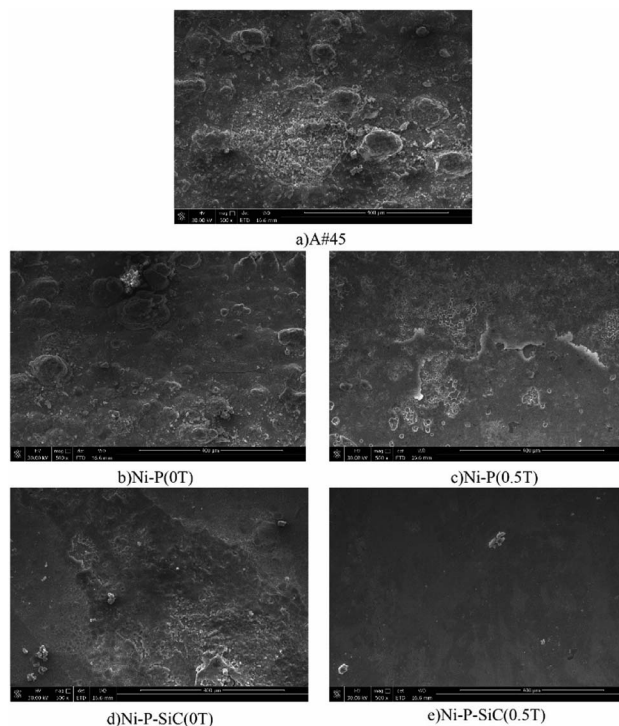
film reduces the area of the coating in contact with the corrosive solution, thereby preventing corrosion.[45] However, the surface film was not complete, and the coating was exposed to the solution at locations of rupture or voids in the film. The electrode potential at the rupture or gaps in the membrane was low, leading to an anodic corrosion of the micro-cells. The Ni–P coating prepared by the conventional jet electrodeposition grew rapidly, and the reaction of the hydrogen evolution on the cathode surface was violent. Therefore, the coating contained pits, cracks, bumps, and other defects. Corrosion may also begin at these defects. Fig. 11c shows the morphology of the Ni–P (0.5 T) coating after corrosion. As shown, the surface corrosion of the coating is uniform, and there are no evident defects such as falling off or cracking. This is because after the addition of the parallel magnetic field, the P element content in the coating increased, and the element distribution was more uniform. When corrosion occurs in a neutral solution, the resistance of a coating increases with the increase in the P content, and corrosion will first occur in low P-content areas.[46]

Table 5 Fitted corrosion parameters for Ni–P–SiC composite coatings

Sample	R_1 (Ω cm²)	R_2 (Ω cm²)	R_3 (Ω cm²)	CPE_1/F	CPE_2/F	Error range (%)
45# steel	6.750		126.8	0.002046		<5.53
Ni–P (0 T)	9.059	52.40	193.3	0.006724	0.01046	<6.57
Ni–P (0.5 T)	7.314	36.67	596.2	0.000189	0.00045	<7.97
Ni–P/SiC (0 T)	7.059	35.72	291.3	0.000151	0.00058	<2.35
Ni–P/SiC (0.5 T)	4.120	11.89	1374.0	0.000018	0.00017	<5.31

Therefore, the coating corrosion situation was improved. Fig. 11d shows the morphology of the Ni–P/SiC (0 T) coating after corrosion. Compared with the Ni–P (0 T) coating, the corrosion condition of the coating surface is improved: shedding of the coating is observed only in a small area, and fine cracks appear locally; however, many corrosion products remain on the coating surface. This is because the structural defects formed during the electrodeposition process, such as cracks, holes, and pits, were filled after the addition of second-phase nano-SiC particles; therefore, the Ni–P/SiC coating exhibited a better corrosion resistance performance under the same preparation process. Fig. 11e shows the morphology of the Ni–P/SiC (0.5 T) coating after corrosion. Compared with Ni–P/SiC (0 T), the corrosion of the coating surface is significantly improved. The coating has no evident defects after corrosion, and there are fewer corrosion products. This is because the parallel magnetic field helped improve the content and uniformity of the nano-SiC particles in the composite coating. The evenly distributed nano-SiC particles not only reduce the metal area exposed to the corrosive medium, but also make the corrosion mechanism of the coating change from local corrosion to pitting corrosion. Therefore, the Ni–P/SiC (0.5 T) coating exhibited a better corrosion resistance.

3.5 Experimental principle

The effect of applying a parallel magnetic field on the preparation of Ni–P and Ni–P/SiC composite coatings by conventional jet electrodeposition was studied. Fig. 12 and 13 show the surface growth mechanism of the Ni–P and Ni–P/SiC composite coatings prepared by conventional jet electrodeposition, respectively. During the growth, the Ni^{2+} and HPO_3^{2+} ions are subjected to the electric field force and move to the cathode surface, where they undergo a redox reaction to form metal atoms. Because the coating surface is not ideally flat, there are many "needle-like" protrusions on the surface during the deposition. According to Guglielmi's adsorption theory,[41] in the preparation of Ni–P/SiC composite coatings by jet electrodeposition, the particles enter the coating in two steps: in the first step, the particles are coated with the charged ions and solvents, forming a weak adsorption outside the dense layer of the electrode, and this weak adsorption is a reversible process. In the second step, under the action of the interfacial electric field, the particles remove the surface film and enter the dense layer to contact with the electrode, forming a strong adsorption that depends on the electric field, and are then being buried by the growing metal; here, the strong adsorption is irreversible. For weak adsorption, the model holds that the equilibrium between the suspended particles and the particles in the weak adsorption state in the bath is similar to Langmuir isothermal
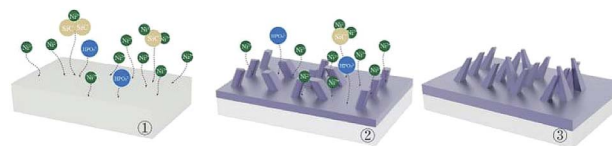

Fig. 12 Mechanism of Ni–P jet electrodeposition.

Fig. 13 Mechanism of Ni–P/SiC jet electrodeposition.

adsorption. Therefore, the form of Langmuir adsorption isothermal can be applied to the mathematical treatment of the weak adsorption step. For the strong adsorption step, the model suggests that the strong adsorption velocity of the particles is related to the electric field between the electrode and the solution interface and the weak adsorption coverage rate. Accordingly, the mathematical expression is deduced as follows:

$$\frac{a}{1-a} = \frac{nFdv_0}{Wi_0} \times e^{(B-A)\eta} \times \frac{kc}{1+kc} \quad (3)$$

where a is the particle eutectoid, η is the electrode over-potential, c is the concentration of the particles suspended in the liquid phase, i_0 is the exchange current density, k is a constant related to the strength of the particle–electrode interaction v_0, A and B are constants determined experimentally, F is Faraday's constant, d is the density of the deposited metal, n is the valence number of the metal ions, and W is the relative atomic weight of the metal.

Guglielmi's model suggests that a reduction of the metal ions adsorbed onto the surface of the particles leads to a composite deposition of the particles. Here, the reduction of the ions on the particle surface is the speed control step, and once the adsorbed ions have undergone an electrochemical reduction reaction on the cathode surface, a co-deposition will occur. In this study, during the preparation of the Ni–P/SiC composite coating by jet electrodeposition, the nano-SiC particles adsorbed the Ni ions moving freely in the bath and moved to the cathode surface together. However, during this movement, the nano-SiC particles were also adsorbed near the nano-SiC particles to form larger aggregates. These large agglomerated particles tended to break through the nanoscale. As the specific surface area of the agglomerated particles decreased significantly, the surface adsorption capacity of the particles weakened; therefore, some of the agglomerated nanoparticles adsorbed only few Ni ions on the surface. After the agglomerated nanoparticles reached the cathode surface, there were few metal atoms on the surface. Therefore, the agglomerated nanoparticles easily moved away from the coating under bath washing. Thus, there were few nanoparticles on the cathode surface in the strong adsorption stage, and the distribution of the nanoparticles in the coating was uneven.

After the addition of the parallel magnetic field, the surface morphology of the cathode changed from rough to smooth as the deposition progressed. Moreover, the co-deposition of the non-conductive nano-SiC particles disturbed the current. The current line deviated, and a component of the current appeared perpendicular to the direction of the magnetic field. Under the action of the current component and magnetic field, a micro-
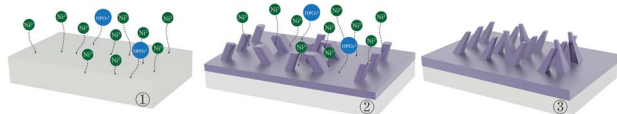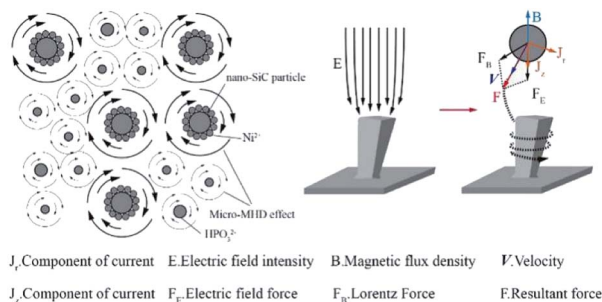
Fig. 14 Mechanism of jet electrodeposition under a magnetic field applied in a direction parallel to the current direction.
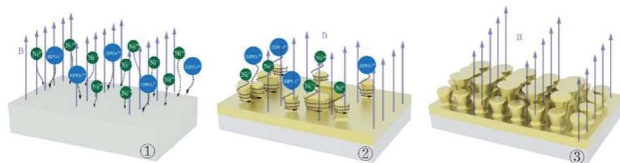

Fig. 15 Mechanism of Ni–P jet electrodeposition under a magnetic field applied in a direction parallel to the current direction.

MHD flow was generated in the area near the cathode. Fig. 14 shows the formation mechanism of the MHD effect near the "protrusions" on the cathode surface during the parallel magnetic field-enhanced jet electrodeposition. The current line morphology of the convex grain front end on the cathode surface is shown in the figure. At this point, a current component J_r, which is perpendicular to the magnetic flux density B, was generated by the electroplating current. According to Lorentz force formula:[47]

$$F_B = B \times J_r \qquad (4)$$

Under the combined action of the Lorentz force and electric field force, eddy currents were generated at the front end of the protrusions.

Fig. 15 and 16 show the surface growth mechanism of the Ni–P and Ni–P/SiC composite coatings prepared by magnetic field-enhanced jet electrodeposition. As the cathode is a soft magnetic material, a gradient magnetic field is generated at the front end of the protrusions. Under the combined action of the gradient magnetic field force and MHD effect, the micro-flow of the bath occurs in the area near the cathode. The bath produces a scouring effect on the front end of the protrusions.[43] This inhibits the normal growth of the inner cells of the coating and prevents the growth of the "needle-like" protrusions, thereby flattening the protrusion front. Thus, the overgrowth of the crystal cells in the vertical direction is effectively prevented, so as to improve the surface quality and performance of the coating. During the growth of the composite coatings, the Ni and HPO_3 ions in the plating solution were subjected to the combined action of the electric field force and Lorentz force, and they had a greater kinetic energy. Moreover, their motion
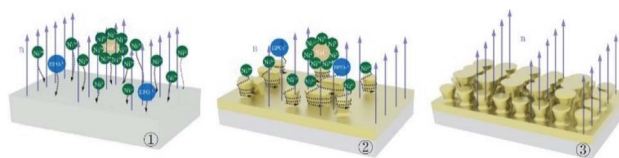

Fig. 16 Mechanism of Ni–P/SiC jet electrodeposition under a magnetic field applied in a direction parallel to the current direction.

trajectory was no longer linear, but spiraled around the grain uplift. Under the action of this "micro-agitation," the composite coating was more compact. At the same time, as 45# steel is a ferromagnetic matrix metal, magnetization will occur under the action of the parallel magnetic field. The metal ions in the plating bath will be affected by the magnetic matrix metal in the deposition process, and get easily deposited on the substrate surface in the lowest energy state, thus making the coating more compact with fewer defects. In the deposition process, the nano-SiC particles were also affected by the eddy current, the self-motion of the particles was enhanced, the polymerization trend between the nanoparticles was weakened, and the nanoparticles were well covered by the Ni ions. Therefore, under the action of the parallel magnetic field, the Ni–P/SiC coating was evenly distributed with the nano-SiC particles and had a good binding force.

4. Conclusion

In this study, composite coatings of Ni–P and Ni–P/SiC were prepared using the jet electrodeposition technology. The influences of applying a magnetic field during the deposition process on the micro-morphology, structure, and composition of the composite coatings were investigated, and the corrosion resistance of the coatings was characterized. The conclusions drawn from the study are as follows:

(1) Ni–P and Ni–P/SiC composite coatings showed a typical cellular structure. Compared with the coating prepared by conventional jet electrodeposition, the surface flatness and quality of the coating prepared under the assistance of the magnetic field were better.

(2) Ni–P and Ni–P/SiC composite coatings exhibited amorphous structures. Compared with the coating prepared by conventional jet electrodeposition, the P fraction of the Ni–P coating prepared by jet electrodeposition increased to 6.45%, and the Si fraction of the Ni–P/SiC composite coating reached 7.02% and was more evenly distributed under the assistance of the magnetic field.

(3) Compared with conventional jet electrodeposition, the Ni–P and Ni–P/SiC composite coatings prepared under the assistance of a magnetic field exhibited a higher corrosion potential, lower corrosion current, and greater equivalent impedance, thus showing an excellent corrosion resistance performance.

Conflicts of interest

There are no conflicts to declare.

Acknowledgements

References

1 X. Zhao, X.-l. Yang and T.-f. Jing, *J. Iron Steel Res. Int.*, 2012, **19**, 75–78.

2 G. Hu, K. Zhang, S. Huang and J.-W. W. Ju, *Acta Mech. Solida Sin.*, 2012, **25**, 348–360.

3 L. Zhu, S. Wang, H. Pan, C. Yuan and X. Chen, *J. Manuf. Process*, 2020, **49**, 344–354.

4 G. Huang, L. Qu, Y. Lu, Y. Wang, H. Li, Z. Qin and X. Lu, *Vacuum*, 2018, **153**, 39–42.

5 W. Cai, F. Meng, X. Gao and J. Hu, *Appl. Surf. Sci.*, 2012, **261**, 411–414.

6 P. Jin, C. Sun, Z. Zhang, C. Zhou and T. Williams, *Surf. Coat. Technol.*, 2020, 125738.

7 B. Li, T. Mei, D. Li and S. Du, *Ultrason. Sonochem.*, 2019, **58**, 104680.

8 F. Xia, Q. Li, C. Ma, W. Liu and Z. Ma, *Ceram. Int.*, 2020, **46**, 7961–7969.

9 A. Rasooli, M. S. Safavi, F. Babaei and A. Ansarian, *J. Alloys Compd.*, 2020, **822**, 153725.

10 B. Li, W. Zhang, D. Li and J. Wang, *Mater. Chem. Phys.*, 2019, **229**, 495–507.

11 M. M. Islam, I. Abdellaoui, C. Moslah, T. Sakurai, M. Ksibi, S. Hamzaoui and K. Akimoto, *Thin Solid Films*, 2018, **654**, 1–10.

12 R. Li, Y. Hou, B. Liu, D. Wang and J. Liang, *Electrochim. Acta*, 2016, **222**, 1272–1280.

13 P. Jin, C. Sun, C. Zhou, L. Shi and C. Liu, *Ceram. Int.*, 2019, **45**, 20155–20164.

14 C. Liu, X. Chang, Y. Wu, X. Wang and X. Hou, *Vacuum*, 2020, **177**, 109430.

15 P. Wang, S. Li, X. Geng, J. Zhang, F. Meng, L. Zhou, H. Sun, X. Li, G. Wen and C. Wei, *J. Alloys Compd.*, 2020, **843**, 156084.

16 C. Ma, D. Zhao and Z. Ma, *Ceram. Int.*, 2020, **46**, 12128–12137.

17 M. Xu, L. Shen, W. Jiang, F. Zhao, Y. Chen and Z. Tian, *J. Alloys Compd.*, 2019, **799**, 224–230.

18 M. Khan, H. Pawar, M. Kumari, C. Patra, G. Patel, U. K. Dwivedi and D. Rathore, *J. Alloys Compd.*, 2020, **840**, 155596.

19 S. Li, W. Yao, J. Liu, M. Yu and K. Ma, *Vacuum*, 2016, **123**, 1–7.

20 A. K. Pradhan and S. Das, *J. Alloys Compd.*, 2014, **590**, 294–302.

21 Y. Shim, L. E. Levine and R. J. Fields, *Physica A*, 2005, **348**, 1–15.

22 T. M. Al-Dhire, H. Zuhailawati and A. S. Anasyida, *Mater. Today: Proc.*, 2019, **17**, 664–671.

23 Y. Yang and Y. Liu, *J. Mater. Sci. Technol.*, 2010, **26**, 1016–1020.

24 R. Ji, K. Han, H. Jin, X. Li, Y. Liu, S. Liu, T. Dong, B. Cai and W. Cheng, *J. Manuf. Process*, 2020, **57**, 787–797.

25 W. Jiang, L. Shen, M. Qiu, X. Wang, M. Fan and Z. Tian, *J. Alloys Compd.*, 2018, **762**, 115–124.

26 D. Ning, A. Zhang, M. Murtaza and H. Wu, *J. Alloys Compd.*, 2019, **777**, 1245–1250.

27 W. Cui, K. Wang, K. Wang and P. Wang, *Ceram. Int.*, 2018, **44**, 7214–7220.

28 F. Xiu-qing, L. Mo-qi, L. Jin-ran, W. Xing-sheng, W. Qing-qing and X. Ye, *Int. J. Electrochem. Sci.*, 2020, **15**, 816–829.

29 M. Shen, X. Fu, X. Wang, J. Lin and Q. Wang, *Nanosci. Nanotechnol. Lett.*, 2019, **11**, 938–946.

30 R. Sen, S. Das and K. Das, *Surf. Coat. Technol.*, 2011, **205**, 3847–3855.

31 Y. Wang, Y. Ju, S. Wei, W. Lu, B. Yan and W. Gao, *Mater. Charact.*, 2015, **102**, 189–194.

32 S. Ghosh, N. Ofori-Opoku and J. E. Guyer, *Comput. Mater. Sci.*, 2018, **144**, 256–264.

33 V. S. Nikitin, T. N. Ostanina, V. M. Rudoi, T. S. Kuloshvili and A. B. Darintseva, *J. Electroanal. Chem.*, 2020, **870**, 114230.

34 C. Zhong, W. B. Hu and Y. F. Cheng, *J. Power Sources*, 2011, **196**, 8064–8072.

35 Y. Yang and Y. F. Cheng, *Electrochim. Acta*, 2013, **109**, 638–644.

36 S. Banthia, S. Sengupta, S. Das and K. Das, *Surf. Coat. Technol.*, 2019, **374**, 833–844.

37 W. Jiang, L. Shen, M. Xu, Z. Wang and Z. Tian, *J. Alloys Compd.*, 2019, **791**, 847–855.

38 S. Dehgahi, R. Amini and M. Alizadeh, *J. Alloys Compd.*, 2017, **692**, 622–628.

39 W. Gao and X. Wang, *J. Magn. Magn. Mater.*, 2019, **483**, 196–204.

40 V. Georgescu and M. Daub, *Surf. Sci.*, 2006, **600**, 4195–4199.

41 N. Guglielmi, *J. Electrochem. Soc.*, 1972, **119**, 1009.

42 Z. P. Liang, Y. Y. Wang, H. Jin, X. Y. Zhou and X. L. Liu, *Rare Met. Cem. Carbides*, 2018, **46**, 59–63, 67.

43 Y. Huang, X. Wu, L. Nie, S. Chen, Z. Sun, Y. He and W. Liu, *Solid State Ionics*, 2020, **345**, 115171.

44 E. Berretti, N. Calisi, A. Capaccioli, L. Capozzoli, A. M. S. Hamouda, A. Giaccherini, W. Giurlani, A. Ienco, S. Martinuzzi, M. Innocenti, U. Waware, S. Virtanen, G. Zangari, R. Ahmed and A. Lavacchi, *Corros. Sci.*, 2020, **175**, 108898.

45 Q.-Q. He, M.-J. Zhou and J.-M. Hu, *Electrochim. Acta*, 2020, **355**, 136796.

46 W. Liu, J. Liu, H. Pan, F. Cao, Z. Wu, H. Lv and Z. Xu, *J. Alloys Compd.*, 2020, **834**, 155095.

47 D. S. Correnti, *Results Phys.*, 2018, **9**, 832–841.